Journal of Power Sources 193 (2009) 530–540

Contents lists available at ScienceDirect

Journal of Power Sources

journal homepage: www.elsevier.com/locate/jpowsour

Microstructure and polarization characteristics of anode supported tubular solid oxide fuel cell with co-precipitated and mechanically mixed Ni-YSZ anodes

Naoki Shikazono*, Yusuke Sakamoto, Yu Yamaguchi, Nobuhide Kasagi

Department of Mechanical Engineering, The University of Tokyo, Hongo 7-3-1, Bunkyo-ku, Tokyo 113-8656, Japan

ARTICLE INFO

Article history:
Received 30 January 2009
Received in revised form 17 April 2009
Accepted 18 April 2009
Available online 3 May 2009

Keywords:
Solid oxide fuel cell
Anode support
Microstructure
Stereology
Image processing

ABSTRACT

An anode support tubular solid oxide fuel cell (SOFC) is fabricated and the dependence of its polarization resistance on anode microstructural parameters is investigated by means of stereology and concept of contiguity (c-c) theory. Nickel yttria-stabilized zirconia (Ni-YSZ) anode supported cell with YSZ electrolyte, lanthanum–strontium–manganite (LSM)-YSZ composite cathode, and LSM cathode layers is fabricated by dip coating. Submicrometer resolution images of anode microstructure are successfully obtained by low voltage SEM-EDX and quantified by stereological analysis. Cell voltage measurements and impedance spectroscopy are performed at temperatures of 650 and 750 °C with hydrogen and nitrogen mixture gas as a fuel. A quantitative relationship between polarization resistance and microstructural parameters such as circularity, three-phase boundary length, contiguity, etc. is investigated using the concept of contiguity (c-c) theory. The effectiveness of correlating polarization resistance of anode supported tubular SOFC using stereology and c-c theory is evaluated.

1. Introduction

Solid oxide fuel cell (SOFC) is one of the most promising energy conversion technologies due to its high efficiency and fuel flexibility [1]. In order to reduce manufacturing cost and to achieve high reliability, recent activities are shifting to operate SOFCs at intermediate temperatures. Anode supported SOFCs have attracted much research interests since they can reduce the electrolyte thickness as well as the electrolyte resistance at low temperature operation [2–4]. Great efforts have been paid for developing materials with high conductivities and electrodes with optimal microstructures to improve the electrode polarization characteristics at low temperature operation.

Porous cermets (such as Ni-YSZ composite) are widely used as anode materials in order to match the thermal expansion coefficient with that of the electrolyte and to extend effective reaction sites (three-phase boundary, TPB) [5]. It is well known that anode microstructure has significant impact on cell performance and durability [6–10]. To date, great efforts have been made to improve anode performance by modifying the anode microstructures. For example, effects of morphology improvement [9,10], dependence on starting materials and fabrication methods [11–13] have been reported. Recently, direct measurements of SOFC electrode microstructures have been reported using focused ion beam scanning electron microscopy (FIB-SEM) [14] and X-ray computed tomography (XCT) [15]. Through these direct measurements, important microstructural parameters such as three-phase boundary length and tortuosity factor can be obtained. However, huge efforts are required for obtaining large amount of data volume with very high resolution for statistical processing. A methodology that can quantify microstructural parameters from two-dimensional microscopy images is preferred especially from the designing point of view. The microstructural parameters such as phase contiguity and effective conductivities can be evaluated from two-dimensional images using stereological theory [16] and concept of contiguity theory [17,18]. Simwonis et al. [19] and Lee et al. [20–23] have applied stereological theory to Ni-YSZ cermets and investigated the contiguity of the phases. Effects of Ni agglomeration, Ni contents or compaction pressure on the effective conductivity of the Ni-YSZ cermet are reported. However, such approach for the electrodes of the real cell configuration is still limited. And more importantly, the quantitative relationship between the microstructural parameters and the polarization resistances is not fully investigated. Thus, quantitative investigation between anode microstructural parameters and polarization characteristics for the real anode supported cell configurations is strongly demanded.

* Corresponding author. Tel.: +81 5841 8850; fax: +81 5841 8850.
E-mail address: shika@feslab.t.u-tokyo.ac.jp (N. Shikazono).

0378-7753/$ – see front matter © 2009 Elsevier B.V. All rights reserved.
doi:10.1016/j.jpowsour.2009.04.031

Nomenclature

a	electrode total thickness (μm)
A_i	average area of phase i (μm^2)
C_i	contiguity of phase i
CPE	constant phase element
d_i	equivalent diameter of phase i (μm)
F	Faraday constant: 9.649 × 104 (C mol^{-1})
i	current density (A cm^{-2})
l_i	mean intercept length of phase i (μm)
L_{TPB}	three-phase boundary length per unit volume (μm μm^{-3})
N_{i-j}	number of contact points of phases i and j per unit length (μm^{-1})
N_{TPB}	number of intersection points of three phases per unit area (μm^{-2})
P_i	average perimeter of phase i (μm)
R	resistance (Ω m)
R_0	gas constant: 8.314 (J mol^{-1} K^{-1})
R_i	circularity of phase i
S_i	total interfacial area of phase i per unit volume (μm^2 μm^{-3})
S_{i-j}	interfacial area of phases i and j per unit volume (μm^2 μm^{-3})
T	temperature (K)
V_i	volume fraction of phase I

Greek symbols

ε	porosity (=V_{pore})
Γ	Thiele modulus
σ	conductivity (S m^{-1})

Subscripts and superscripts

eff	effective value in multi phase media
el	electron
io	ion
h	high frequency
l	low frequency
ohm	ohmic
i	phase i (Ni, YSZ-pore)
Ni	nickel phase
Pore	pore phase
YSZ	YSZ phase
TPB	three-phase boundary

In the present work, microstructure of the tubular anode supported SOFC is quantified and the effects of anode microstructure on its polarization resistances are evaluated. To obtain cells with different anode microstructures, two different NiO-YSZ starting materials are used and the amounts of poreformer were varied. Then, electrolyte and cathode layers were dip coated onto the anode supports. *I–V* curves and Nyquist plots were obtained at temperatures of 650 and 750 °C using hydrogen and nitrogen mixture gas as a fuel. Reduced anode microstructures were imaged using low voltage scanning electron microscopy (SEM) with energy dispersive X-ray spectroscopy (EDX). Microstructural parameters such as three-phase boundary (TPB) length and contiguity are quantified by means of stereology [16]. The effects of starting material and poreformers on microstructure are evaluated. Finally, the relationship between the anode microstructural parameters and the polarizations is investigated using concept of contiguity theory [17–19].

2. Cell fabrication

Anode supported cells used in the present study consist of Ni-YSZ anode support (thickness 500 μm), YSZ electrolyte (20 μm), LSM-YSZ composite (10 μm) and LSM cathode current collector (10 μm) layers. NiO-YSZ (60/40 vol%) powders (AGC Seimi Chemical Co., Ltd.) with binder (methylcellulose) were mixed and extruded into a tubular shape (Kankyo Ceramics Research Co. Ltd., Japan). Since sintering shrinkage rate is sensitive to the amount of poreformers, anode pre-sintering temperature was chosen differently (1100 or 1200 °C) for the cells depending on the anode microstructures so that every cell has nearly the same electrolyte thickness. Then, YSZ slurry was dip coated on the anode support, and co-sintered at 1400 °C for 3 h. The LSM-YSZ (50/50 wt%) composite cathode layer and LSM cathode current collector layer were dip coated and sintered at 1200 and 1100 °C for 3 h, respectively. Finally, Ag wire was connected to the cell by Ag paste. Anode side current collection wire was connected to one edge of the anode support. After connecting the cell with the fuel supply tube, the sealant (Dura Seal 1529 UHT, Cotronics Corp.) was painted over the anode with the current collection wire for perfect sealing. Fig. 1 shows the schematic of the fabricated anode supported cell.

To change the anode porosity, the amount of acrylic poreformer (1.5 μm, Soken Chemical & Engineering Co., Ltd.) was varied as 0 wt%, 9 wt% and 17 wt%. For the starting materials, co-precipitated or mechanically mixed NiO-YSZ powders were employed. The mean grain size of the mechanically mixed powders was around 1 μm. Primary particle size of the co-precipitated powders is 30–50 nm and they were uniformly distributed inside the secondary grains around 1 μm. Table 1 shows the specifications of the cells tested in this study. Fig. 2 illustrates the cross-section of the fabricated co-precipitated cell with 17 wt% poreformer (C-17 wt% cell).

The cells were connected to the fuel supply tube with adhesion bond (904 Zirconia, Cotronics Corp.) and sealant (Dura Seal 1529 UHT, Cotronics Corp.). Ag wires were connected to the electronic load controller (Kikusui Electronics Corp., PLZ664) and impedance meter (Kikusui Electronics Corp., KFM2150).

The anode was reduced in H_2 20 sccm and N_2 10 sccm at 750 °C for 10 h. The ramp rate was 10 °C min^{-1} in all heating and cooling processes. Hydrogen/nitrogen flow rates were set as 20/10 or 2/28 sccm fixing the total flow rate at 30 sccm. Air flow rate was fixed as 20 slm. Then, *I–V* curves and Nyquist plots were acquired at temperatures of 650 and 750 °C.

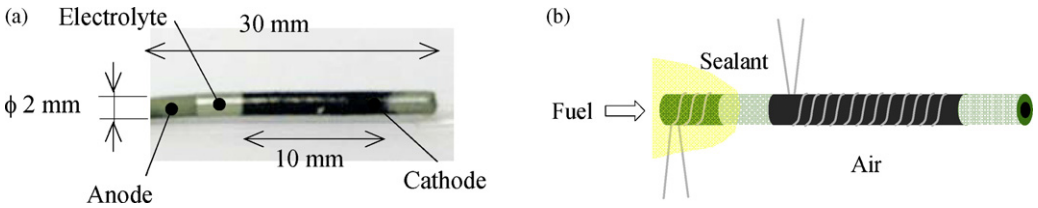

Fig. 1. Schematic of the fabricated cell.

Table 1
Fabricated anode samples.

Abbreviation	Starting NiO/YSZ powder	NiO/YSZ ratio (wt%)	Amount of poreformer (wt%)	Pre-sintering temperature (°C)	Co-sintering temperature (°C)
C-0 wt%	Co-precipitation	60/40	0	1200	1400
C-9 wt%	Co-precipitation	60/40	9	1100	1400
C-17 wt%	Co-precipitation	60/40	17	1100	1400
M-0 wt%	Mechanical mixing	60/40	0	1200	1400
M-9 wt%	Mechanical mixing	60/40	9	1100	1400
M-17 wt%	Mechanical mixing	60/40	17	1100	1400

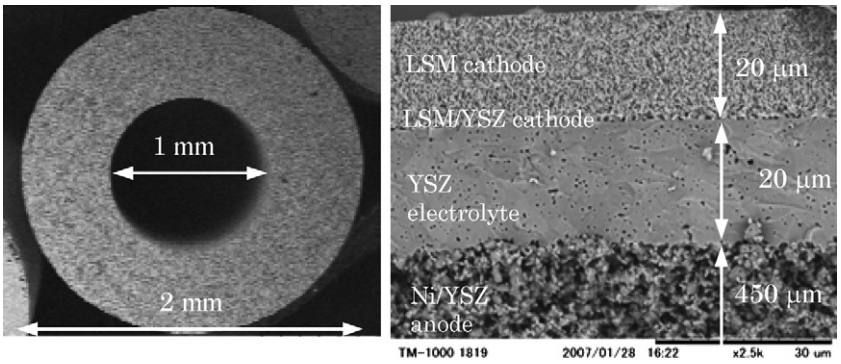

Fig. 2. Cross-section of the fabricated cell (C-17 wt%).

3. Microstructure quantification

3.1. Image processing

Samples were infiltrated with epoxy resin (Marumoto struers K.K.) under vacuum. Cured samples were polished by Ar-ion beam cross-section polisher (JEOL Ltd., SM-09010). This technique provided less damage and smoother cross-section than the diamond slurry polishing. Then, microstructure of the cross-section was successfully imaged by the energy selected backscattered (ESB) electron detector and energy dispersive X-ray spectroscopy (EDX; Thermo Electron, NSS300) in low voltage scanning electron microscopy (SEM; Carl Zeiss, ULTRA55). The size of the images is 30.3 μm × 40.5 μm with 768 × 1024 pixels. As shown in Fig. 3, ESB and EDX of low voltage SEM provided images with submicron resolution. Co-precipitated cells show finer and more complicated structures than the mechanically mixed cells. For image processing, a weighted differential filter was applied to sharpen grain boundaries. Pore was first distinguished from the ESB images, and then solid Ni and YSZ phases were distinguished using the EDX images. Fig. 4 shows the processed images of the six samples listed in Table 1. As can be seen from the figure, Ni (white), YSZ (gray) and pore (black) phases are clearly distinguished.

From these processed images, volumetric fraction V_i, area A_i, perimeter P_i, mean intercept length l_i of each phase, number of contact points of i and j phases per unit length N_{i-j}, number of intersection points of three phases per unit area N_{TPB} are obtained. Diameter d_i and circularity R_i of each phase are calculated as:

$$d_i = 2\sqrt{\frac{A_i}{\pi}}, \tag{1}$$

$$R_i = \frac{P_i^2}{4\pi A_i}. \tag{2}$$

Note that circularity R_i takes larger values as the shape becomes more complicated.

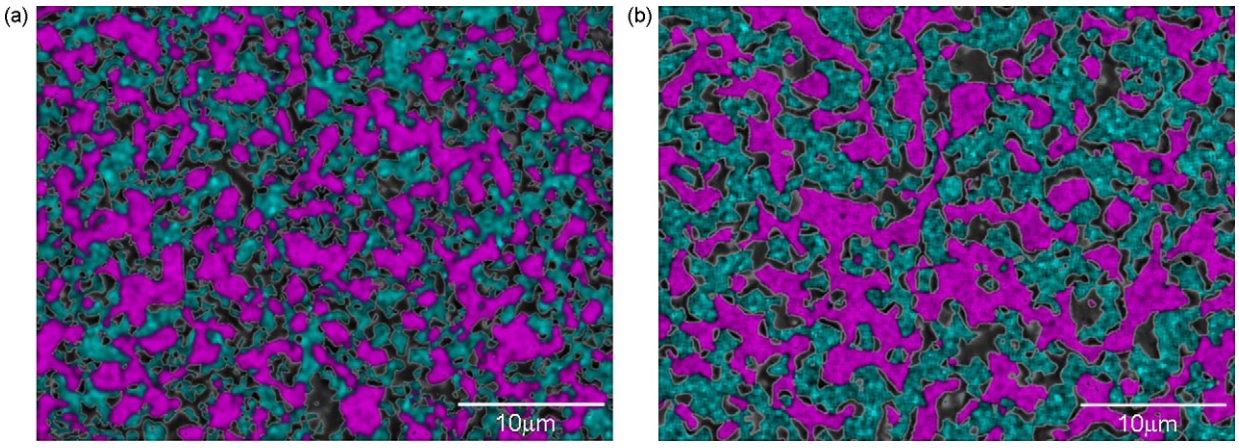

Fig. 3. SEM-EDX images. red: Ni, green: YSZ, black: pore. (a) C-0 wt% cell and (b) M-0 wt% cell. (For interpretation of the references to color in this figure legend, the reader is referred to the web version of the article.)

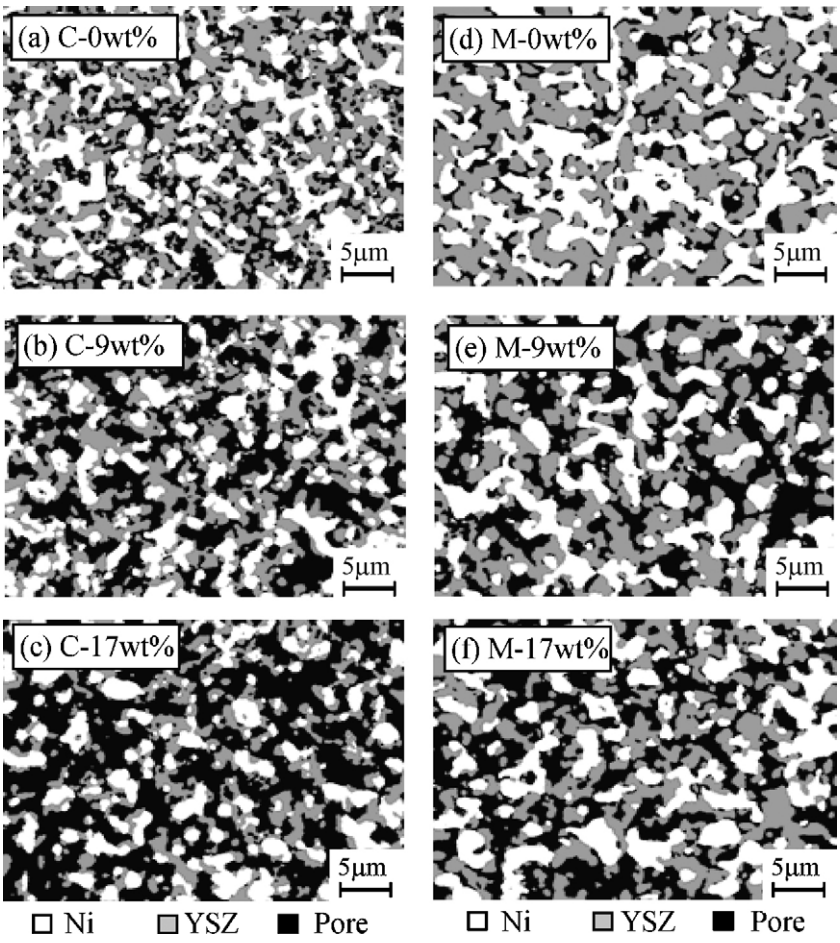

Fig. 4. Processed cross-sectional images of the anodes. Co-precipitated (a)–(c), and mechanically mixed (d)–(f) anodes.

3.2. Stereology

According to the theory of stereology [16], the microstructure information of two-dimensional images can be transformed to three-dimensional information. Interfacial area S_{i-j}, which is the neck area between i and j phases per unit volume, and TPB length L_{TPB} per unit volume in an isotropic structure can be written as:

$$S_{i-j} = 2N_{i-j}, \tag{3}$$

$$L_{TPB} = 2N_{TPB}. \tag{4}$$

Contiguity C_i [17–20] is defined as the fraction of the interfacial area shared with the same phase to the total surface area of the corresponding phase. Simiwonis et al. [19] extended the theoretical approach for the equiaxed two-phase solid to the Ni-YSZ-pore three-phase problem and obtained following expression for contiguity:

$$C_i = \frac{S_i}{S_i + S_j + S_k}, \tag{5}$$

where $S_i = 2S_{i-i} + S_{i-j} + S_{i-k}$ is the total interfacial area of phase i. Volume to surface ratio is related to the intercept length l_i by:

$$\frac{V_i}{S_i} = \frac{l_i}{4}. \tag{6}$$

Then, Eq. (5) can be rewritten in terms of volume fraction V_i and mean intercept length l_i as:

$$C_i = \frac{V_i l_j l_k}{V_i l_j l_k + V_j l_k l_i + V_k l_i l_j}. \tag{7}$$

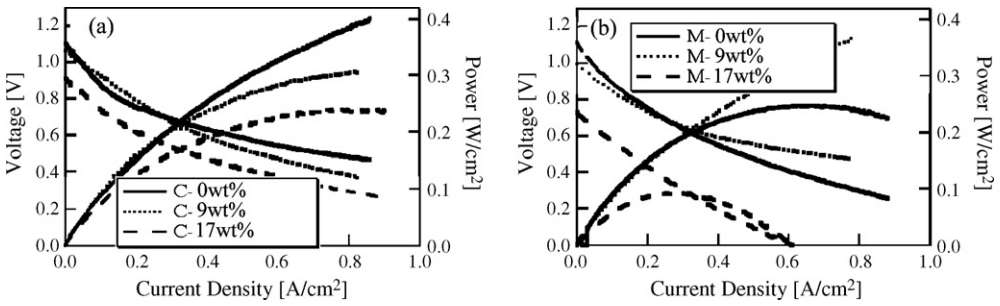

Fig. 5. Performance curves for H_2 = 20 sccm at 750 °C. (a) Co-precipitated and (b) mechanically mixed anodes.

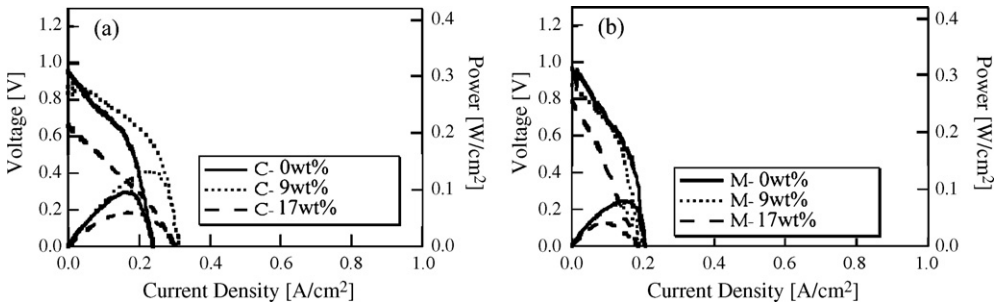

Fig. 6. Performance curves for H_2 = 2 sccm at 750 °C. (a) Co-precipitated and (b) mechanically mixed anodes.

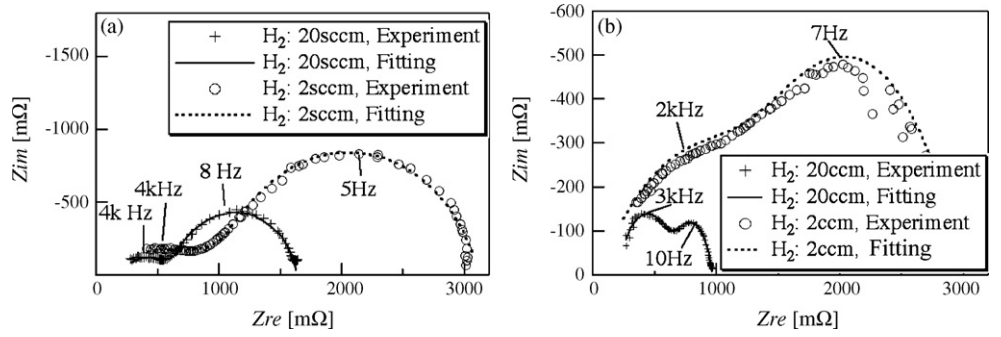

Fig. 7. Impedance spectra at i = 0.16 A cm^{-2}, (a) C-0 wt% and (b) C-9 wt% cells.

Thus, contiguity can be easily obtained from the two-dimensional images through Eq. (7). The effective conductivity will be related to contiguity C_i in the later section.

4. Results and discussion

4.1. Cell testing

A typical example of the obtained voltage and power density curves at 750 °C are shown in Figs. 5 and 6. As shown in Fig. 5, co-precipitated cells shows slightly better performance than the mechanically mixed cells at H_2 = 20 sccm, and the maximum power density (MPD) was over 0.4 W cm^{-2} for the C-0 wt% cell. C-17 wt% and M-17 wt% cells showed low open circuit voltage (OCV). From the SEM images, it is observed that the electrolyte layers of C-17 wt% and M-17 wt% cells were not dense enough, which lead to imperfect sealing. Fig. 6 shows the results for the H_2 = 2 sccm case. Co-precipitated cells again showed better performance than the mechanically mixed cells. Especially, C-9 wt% cell exhibits MPD of 0.15 W cm^{-2} and the maximum fuel utilization exceeded 85%. Effect of poreformers was different depending on the starting materials and the hydrogen flow rates. For the co-precipitated cells, C-0 wt% cell performed better for the H_2 = 20 sccm case, while C-9 wt% cell was better at H_2 = 2 sccm. On the other hand, for the mechanically mixed cells, M-9 wt% cell performed favorably in H_2 = 20 sccm case, while M-0 wt% cell was slightly better at H_2 = 2 sccm.

To separate ohmic, activation, and concentration polarizations, impedance spectroscopy data were obtained at i = 0.16 A cm^{-2}. Fig. 7 shows a typical example of the obtained Nyquist plot. Two semi-circles were least-square fitted to obtain ohmic (R_{ohm}), high frequency (R_h) and low frequency (R_l) resistances. The equivalent electrical circuit is shown in Fig. 8.

The sum of the ohmic resistances of the electrolyte, cathode and anode is measured as R_{ohm}. The high frequency resistance R_h is considered to be due to the activation overpotentials of the anode and the cathode, while the major contribution of the low frequency resistance R_l is due to the concentration polarization [24]. Fig. 9 shows the obtained R_h and R_l of the cells. C-17 wt% cell and M-17 wt% cell data are not plotted in the figure because of the leakage problem described above. As shown in Fig. 9, co-precipitated cells show smaller R_h and R_l than the mechanically mixed cells. Addition of poreformers drastically reduces R_l but increases R_h. Voltage drop due to fuel shortage was apparent at H_2 = 2 sccm, T = 650 °C case around i = 0.1 A cm^{-2}. This may be the reason for the large R_l obtained for the M-9 wt% cell at H_2 = 2 sccm, T = 650 °C in Fig. 9(a).

4.2. Microstructure quantification results

The original 30.3 μm × 40.5 μm images are divided into four 15.2 μm × 20.2 μm sub-regions in order to investigate the dependence of the micro-structural parameters on the analyzed area. The parameters directly obtained from the image processing are listed in Table 2. The mean values as well as the standard deviations of the data from four sub-regions are also shown. As can be seen from Table 2, the standard deviations of the four images are quite large. The standard deviations of the parameters related to the pore phase, e.g. A_{pore} and P_{pore}, are very large, while those for the solid phases remain relatively small. Table 3 shows the parameters calculated from Eqs. (1)–(4) and (7) using the data listed in Table 2. In Fig. 10, equivalent diameters d_i are plotted against porosity ε (=V_{pore}). As the data show quite large scattering, data from four sub-regions are listed in the figure as four independent points with a same symbol. It can be seen from the figure that each of the data sets for the co-precipitated cells and mechanically mixed cells correlates

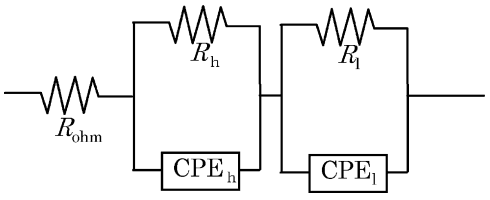

Fig. 8. Equivalent circuit of SOFC anode.

Table 2
Microstructural parameters directly obtained from image processing.

Cell		Volume ratio			Area			Perimeter			Intercept length			Number of contact points of *i* and *j* phases			Interception points of three phases
		V_{Ni}	V_{YSZ}	V_{pore} (=ε)	A_{Ni} (μm^2)	A_{YSZ} (μm^2)	A_{pore} (μm^2)	P_{Ni} (μm)	P_{YSZ} (μm)	P_{pore} (μm)	l_{Ni} (μm)	l_{YSZ} (μm)	l_{pore} (μm)	$N_{Ni\text{-}pore}$ (μm^{-1})	$N_{Ni\text{-}YSZ}$ (μm^{-1})	$N_{YSZ\text{-}pore}$ (μm^{-1})	N_{TPB} (μm^{-2})
C-0 wt%	Image 1	0.375	0.373	0.252	3.291	1.143	0.878	8.343	5.095	4.990	1.251	0.757	0.606	0.413	0.720	1.235	1.017
	Image 2	0.351	0.410	0.239	3.168	1.654	0.611	8.973	6.799	3.557	1.071	0.820	0.596	0.426	0.770	1.235	1.073
	Image 3	0.350	0.393	0.257	2.827	1.746	0.717	7.926	7.520	4.063	1.143	0.742	0.586	0.441	0.724	1.261	1.017
	Image 4	0.322	0.446	0.232	2.147	2.442	0.579	5.826	9.045	3.311	1.128	0.912	0.586	0.346	0.715	1.233	0.939
	Mean	0.350	0.405	0.245	2.858	1.746	0.696	7.767	7.115	3.980	1.148	0.808	0.593	0.406	0.732	1.241	1.011
	σ	0.014	0.019	0.009	0.240	0.325	0.134	0.527	1.246	0.727	0.091	0.042	0.010	0.014	0.028	0.015	0.032
	σ (%)	4.1%	4.6%	3.8%	8.4%	18.6%	19.3%	6.8%	17.5%	18.3%	7.9%	5.2%	1.7%	3.5%	3.8%	1.2%	3.2%
C-9 wt%	Image 1	0.292	0.342	0.366	1.947	1.039	2.079	5.854	4.453	6.890	1.037	0.769	0.979	0.358	0.677	1.049	0.945
	Image 2	0.277	0.304	0.419	1.573	0.881	3.891	4.772	4.121	11.578	0.978	0.727	1.145	0.376	0.635	1.064	0.952
	Image 3	0.292	0.319	0.389	1.826	1.304	2.254	5.142	5.559	6.559	1.176	0.794	1.125	0.349	0.630	0.966	0.815
	Image 4	0.307	0.346	0.346	1.886	1.167	1.380	5.281	5.014	4.862	1.124	0.760	0.941	0.360	0.668	1.098	1.027
	Mean	0.292	0.328	0.380	1.808	1.098	2.401	5.262	4.787	7.472	1.079	0.762	1.048	0.361	0.653	1.044	0.935
	σ	0.009	0.019	0.026	0.191	0.214	1.000	0.550	0.753	2.807	0.102	0.034	0.091	0.014	0.026	0.053	0.077
	σ (%)	3.0%	5.8%	6.9%	10.6%	19.5%	41.6%	10.5%	15.7%	37.6%	9.4%	4.4%	8.7%	3.8%	4.0%	5.1%	8.3%
C-17 wt%	Image 1	0.228	0.220	0.553	1.589	0.629	14.124	4.592	2.956	26.444	1.131	0.692	1.662	0.358	0.427	0.829	0.740
	Image 2	0.234	0.256	0.510	1.563	0.649	6.015	4.376	2.787	12.779	1.098	0.749	1.515	0.358	0.446	0.904	0.769
	Image 3	0.248	0.287	0.465	1.858	0.807	4.193	5.015	3.314	9.443	1.212	0.782	1.426	0.297	0.503	0.918	0.740
	Image 4	0.198	0.279	0.523	1.192	0.822	4.864	4.009	3.715	10.919	0.897	0.722	1.433	0.322	0.489	1.049	0.756
	Mean	0.227	0.260	0.513	1.551	0.727	7.299	4.498	3.193	14.896	1.084	0.736	1.509	0.334	0.466	0.925	0.751
	σ	0.010	0.034	0.044	0.163	0.098	5.287	0.325	0.269	9.009	0.059	0.046	0.119	0.035	0.040	0.048	0.017
	σ (%)	4.6%	13.0%	8.6%	10.5%	13.4%	72.4%	7.2%	8.4%	60.5%	5.4%	6.2%	7.9%	10.5%	8.5%	5.2%	2.3%
M-0 wt%	Image 1	0.408	0.435	0.157	5.960	1.992	0.482	13.246	4.738	3.047	1.432	1.337	0.490	0.521	0.545	0.696	0.971
	Image 2	0.396	0.427	0.177	5.781	2.427	0.654	12.280	5.728	3.857	1.546	1.416	0.581	0.527	0.469	0.736	0.812
	Image 3	0.419	0.393	0.188	8.562	1.676	0.687	15.876	4.133	3.829	1.709	1.321	0.593	0.498	0.393	0.759	0.802
	Image 4	0.315	0.487	0.198	3.333	2.871	0.691	8.153	6.485	3.932	1.364	1.476	0.586	0.479	0.450	0.870	0.773
	Mean	0.384	0.436	0.180	5.909	2.241	0.628	12.389	5.271	3.666	1.513	1.388	0.563	0.506	0.464	0.765	0.839
	σ	0.011	0.022	0.016	1.556	0.377	0.110	1.861	0.805	0.459	0.139	0.051	0.056	0.015	0.076	0.032	0.095
	σ (%)	3.0%	5.1%	8.7%	26.3%	16.8%	17.6%	15.0%	15.3%	12.5%	9.2%	3.6%	10.0%	3.0%	16.3%	4.2%	11.3%
M-9 wt%	Image 1	0.311	0.383	0.306	3.976	1.565	1.880	8.811	4.717	6.755	1.426	1.060	0.894	0.367	0.453	0.908	0.675
	Image 2	0.305	0.328	0.367	4.455	1.005	2.562	9.780	3.317	7.561	1.433	0.992	1.174	0.382	0.426	0.878	0.760
	Image 3	0.270	0.355	0.375	3.314	1.451	2.397	7.467	4.310	6.977	1.293	1.096	1.109	0.366	0.355	0.891	0.649
	Image 4	0.261	0.349	0.390	2.670	1.231	3.416	6.348	3.769	9.893	1.286	1.072	1.141	0.399	0.358	0.903	0.668
	Mean	0.287	0.354	0.360	3.604	1.313	2.564	8.102	4.028	7.797	1.360	1.055	1.079	0.379	0.398	0.895	0.688
	σ	0.022	0.028	0.038	0.573	0.296	0.356	1.161	0.720	0.416	0.079	0.053	0.147	0.009	0.051	0.015	0.058
	σ (%)	7.7%	7.8%	10.5%	15.9%	22.6%	13.9%	14.3%	17.9%	5.3%	5.8%	5.0%	13.6%	2.3%	12.7%	1.6%	8.4%
M-17 wt%	Image 1	0.286	0.289	0.425	4.614	0.963	4.832	9.404	3.448	13.098	1.660	0.899	1.225	0.384	0.299	0.924	0.587
	Image 2	0.292	0.313	0.396	3.579	1.020	3.035	8.562	3.690	9.300	1.293	0.920	1.102	0.446	0.390	0.959	0.717
	Image 3	0.302	0.363	0.335	4.033	1.236	2.186	9.203	3.990	7.370	1.438	1.079	0.985	0.365	0.449	0.937	0.789
	Image 4	0.302	0.374	0.324	3.307	1.383	1.988	7.380	4.201	7.242	1.304	1.108	0.929	0.420	0.401	0.954	0.756
	Mean	0.295	0.335	0.370	3.883	1.151	3.010	8.637	3.832	9.252	1.424	1.001	1.060	0.404	0.385	0.944	0.712
	σ	0.008	0.038	0.046	0.519	0.144	1.351	0.440	0.272	2.915	0.185	0.098	0.120	0.042	0.076	0.018	0.102
	σ (%)	2.9%	11.2%	12.4%	13.4%	12.5%	44.9%	5.1%	7.1%	31.5%	13.0%	9.8%	11.3%	10.4%	19.6%	1.9%	14.4%

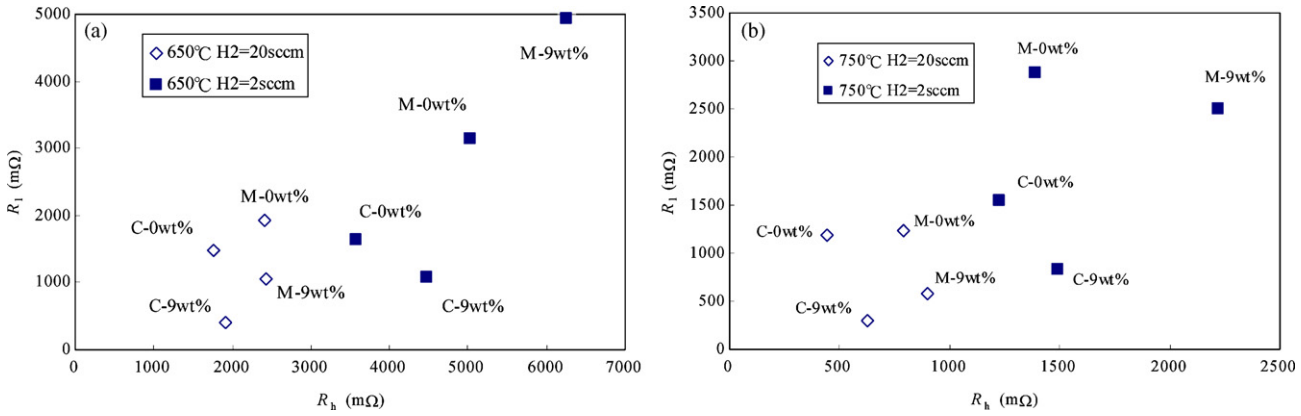

Fig. 9. R_h and R_l from impedance spectroscopy at (a) 650 °C and (b) 750 °C.

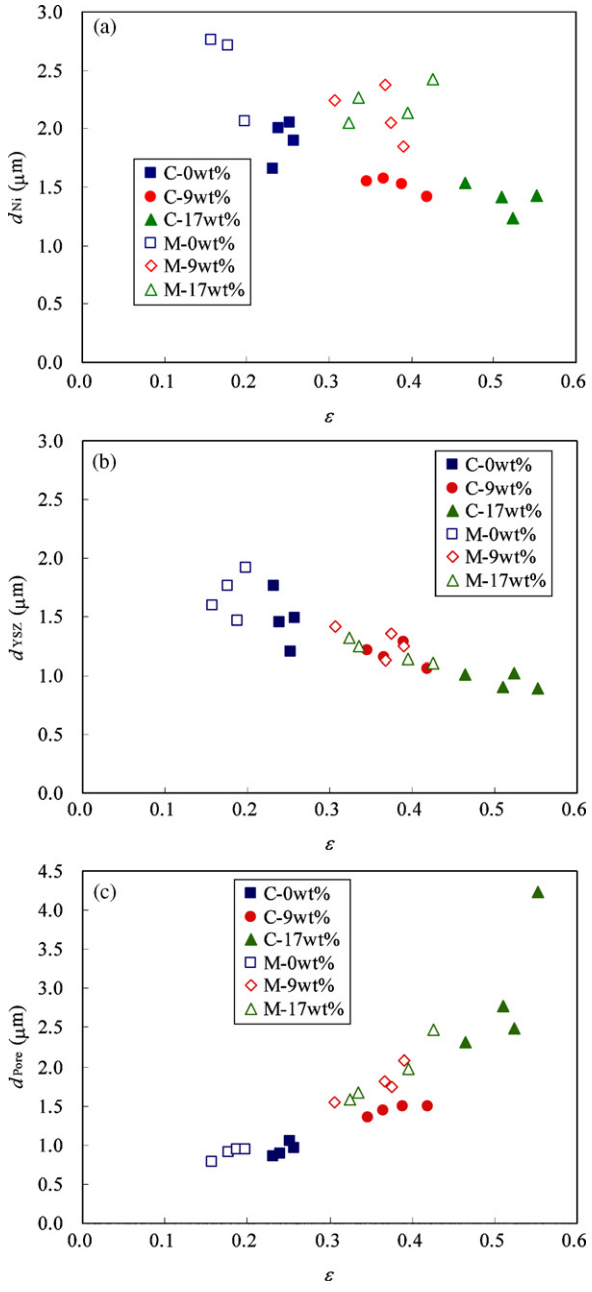

Fig. 10. Equivalent diameter d_i against porosity ε. (a) Ni, (b) YSZ and (c) pore.

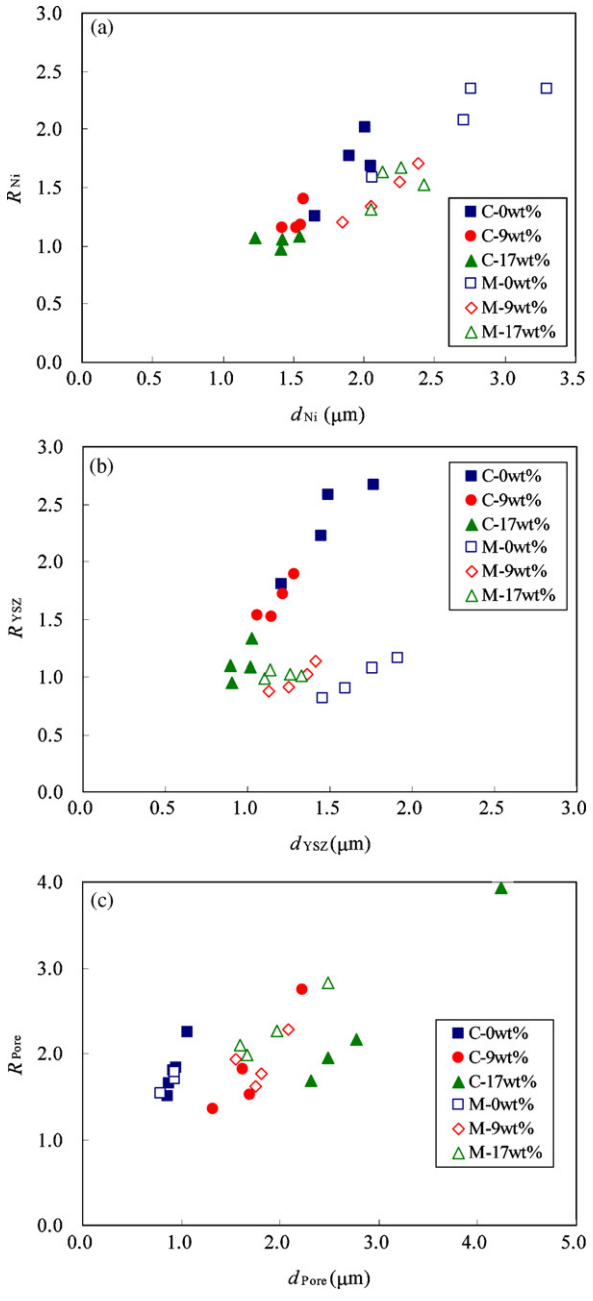

Fig. 11. Relationship between circularity R_i and equivalent diameter d_i. (a) Ni, (b) YSZ and (c) pore.

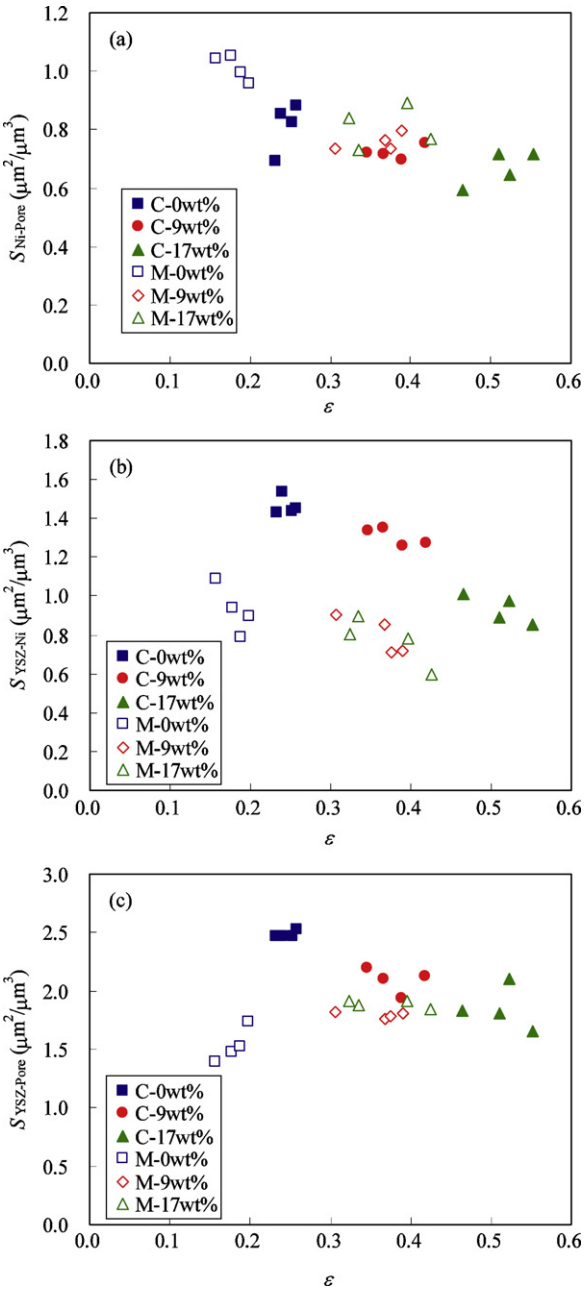

Fig. 12. Interfacial area between different phases S_{i-j}. (a) Ni-pore, (b) YSZ-Ni and (c) YSZ-pore.

quite well with porosity even porosity shows large scattering. This implies that the variation of parameters between the sub-regions is mainly due to the variation of porosity. Thus, even with data dispersion, it is expected that the present data can be used for discussing the differences of microstructural parameters between the cells. Fig. 11 shows the relationship between circularity R_i and equivalent diameter d_i. The mechanically mixed cells have larger Ni diameter d_{Ni} and circularity R_{Ni} than the co-precipitated cells. On the other hand, co-precipitated cells have larger YSZ circularity R_{YSZ} than the mechanically mixed cells. From its definition, larger circularity corresponds to non-circular shape of the phase. These indicate that YSZ phase of the co-precipitated cells is more complicated, while Ni phase of mechanically mixed cells is larger and somewhat agglomerated. No apparent difference between co-precipitated and mechanically mixed cells is observed for the pore circularity R_{pore} in Fig. 11(c). Fig. 12 shows the interfacial area between different phases

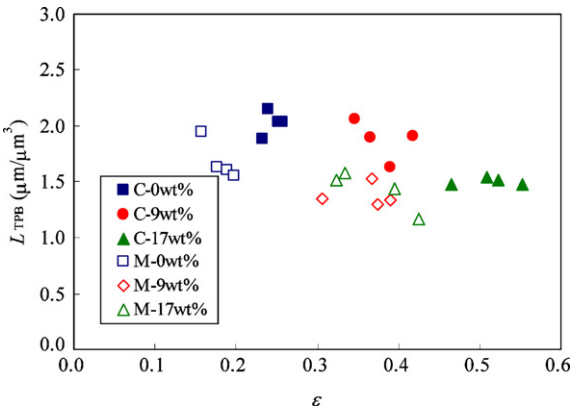

Fig. 13. TPB length L_{TPB} against porosity ε.

S_{i-j}. Again, each of the co-precipitated cell and mechanically mixed cell data is well correlated with porosity. Mechanically mixed cells show slightly larger Ni-pore interfacial area, while co-precipitated cells show larger YSZ–Ni and YSZ-pore interfacial areas. From above results, it can be concluded that good connections of YSZ–YSZ and YSZ–Ni phases are achieved in the co-precipitated cells, while Ni phase is somewhat isolated and agglomerated within the pore for the mechanically mixed cells. Fig. 13 shows the TPB length L_{TPB} and porosity ε (=V_{pore}). Porosity increases but TPB length decreases with increasing the amount of poreformer. Co-precipitated cells have longer TPB length and higher porosity than the mechanically mixed cells. The TPB length L_{TPB} is also plotted against geometric average of the equivalent diameters $(d_{Ni}d_{YSZ}d_{pore})^{1/3}$ in Fig. 14. It can be seen that all L_{TPB} data are well correlated with the average equivalent diameter regardless of starting material. Thus, the large L_{TPB} of co-precipitated cells can be attributed mainly to the fine microstructure, especially to the finer Ni phase as shown in Fig. 10(a). Even the cells are co-fired with the YSZ electrolyte layer at 1400 °C, it is considered that the complicated YSZ network and large interfacial area between YSZ and Ni phases of the co-precipitated cell possibly prevented Ni sintering.

4.3. Polarization resistance and Microstructure

Finally, relationship between polarization resistances and microstructural parameters is discussed. According to Costamagna et al. [25,26], Thiele modulus Γ is defined as:

$$\Gamma = \sqrt{\frac{i_0 L_{TPB} F (1/\sigma_{io}^{eff} + 1/\sigma_{el}^{eff})}{R_0 T}} a, \tag{8}$$

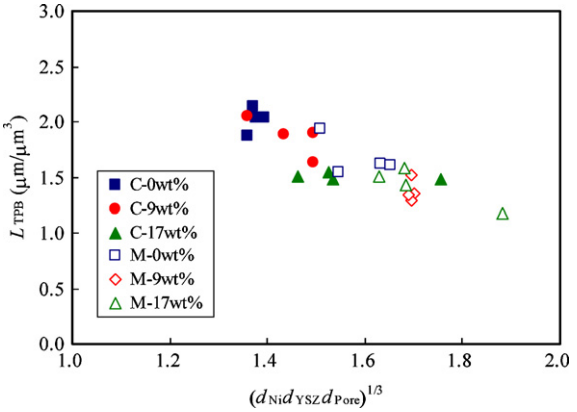

Fig. 14. TPB length L_{TPB} against geometric average of equivalent diameters $(d_{Ni}d_{YSZ}d_{pore})^{1/3}$.

Table 3
Microstructural parameters calculated from Eqs. (1)–(4) and (7).

Cell		Diameter			Circularity			Interfacial area			TPB length	Contiguity		
		d_{Ni} (μm)	d_{YSZ} (μm)	d_{pore} (μm)	R_{Ni}	R_{YSZ}	R_{pore}	$S_{Ni\text{-}pore}$ (μm^2)	$S_{Ni\text{-}YSZ}$ (μm^2)	$S_{YSZ\text{-}pore}$ (μm^2)	L_{TPB} (μm^2 μm^{-3})	C_{Ni}	C_{YSZ}	C_{pore}
C-0 wt%	Image 1	2.047	1.206	1.058	1.683	1.808	2.256	0.825	1.440	2.470	2.034	0.248	0.407	0.344
	Image 2	2.008	1.451	0.882	2.022	2.225	1.646	0.852	1.540	2.471	2.145	0.267	0.406	0.327
	Image 3	1.897	1.491	0.955	1.768	2.578	1.833	0.882	1.448	2.522	2.034	0.240	0.415	0.344
	Image 4	1.653	1.763	0.859	1.258	2.666	1.505	0.692	1.430	2.465	1.878	0.244	0.418	0.339
	Mean	1.902	1.478	0.939	1.683	2.319	1.810	0.813	1.465	2.482	2.023	0.250	0.412	0.338
	σ	0.078	0.154	0.088	0.176	0.385	0.312	0.028	0.055	0.030	0.064	0.014	0.005	0.010
	σ (%)	4.1	10.4	9.4	10.5	16.6	17.3	3.5	3.8	1.2	3.2	5.4	1.2	3.0
C-9 wt%	Image 1	1.575	1.150	1.627	1.400	1.519	1.818	0.717	1.354	2.099	1.891	0.256	0.404	0.340
	Image 2	1.415	1.059	2.226	1.152	1.534	2.741	0.752	1.271	2.127	1.904	0.265	0.392	0.342
	Image 3	1.525	1.289	1.694	1.152	1.885	1.519	0.697	1.259	1.932	1.630	0.249	0.403	0.348
	Image 4	1.550	1.219	1.325	1.177	1.714	1.364	0.720	1.336	2.196	2.054	0.249	0.415	0.336
	Mean	1.516	1.179	1.718	1.220	1.663	1.860	0.722	1.305	2.089	1.870	0.255	0.404	0.341
	σ	0.082	0.116	0.328	0.143	0.207	0.637	0.028	0.052	0.106	0.154	0.008	0.007	0.004
	σ (%)	5.4	9.8	19.1	11.8	12.5	34.3	3.8	4.0	5.1	8.3	3.2	1.6	1.2
C-17 wt%	Image 1	1.422	0.895	4.241	1.056	1.105	3.940	0.716	0.854	1.659	1.480	0.237	0.373	0.390
	Image 2	1.411	0.909	2.767	0.975	0.953	2.161	0.715	0.892	1.809	1.539	0.239	0.383	0.378
	Image 3	1.538	1.014	2.311	1.077	1.083	1.692	0.595	1.007	1.836	1.480	0.228	0.409	0.363
	Image 4	1.232	1.023	2.489	1.073	1.337	1.951	0.644	0.978	2.098	1.513	0.227	0.397	0.376
	Mean	1.401	0.960	2.952	1.045	1.119	2.436	0.668	0.933	1.850	1.503	0.233	0.390	0.377
	σ	0.070	0.065	1.009	0.054	0.082	1.186	0.070	0.079	0.096	0.034	0.006	0.018	0.014
	σ (%)	5.0	6.8	34.2	5.2	7.3	48.7	10.5	8.5	5.2	2.3	2.5	4.7	3.6
M-0 wt%	Image 1	2.755	1.592	0.783	2.343	0.897	1.534	1.043	1.090	1.391	1.943	0.306	0.350	0.344
	Image 2	2.713	1.758	0.913	2.076	1.076	1.809	1.054	0.937	1.471	1.623	0.297	0.350	0.353
	Image 3	3.302	1.461	0.935	2.343	0.811	1.699	0.996	0.787	1.518	1.604	0.285	0.346	0.369
	Image 4	2.060	1.912	0.938	1.587	1.166	1.780	0.958	0.899	1.741	1.545	0.257	0.367	0.376
	Mean	2.707	1.681	0.892	2.087	0.987	1.705	1.013	0.928	1.530	1.679	0.286	0.353	0.361
	σ	0.328	0.149	0.082	0.154	0.135	0.138	0.031	0.151	0.064	0.190	0.011	0.002	0.013
	σ (%)	12.1	8.9	9.2	7.4	13.7	8.1	3.0	16.3	4.2	11.3	3.7	0.6	3.5
M-9 wt%	Image 1	2.250	1.411	1.547	1.554	1.132	1.932	0.735	0.906	1.815	1.350	0.237	0.391	0.372
	Image 2	2.382	1.131	1.806	1.708	0.871	1.776	0.765	0.853	1.757	1.519	0.249	0.386	0.366
	Image 3	2.054	1.359	1.747	1.339	1.019	1.616	0.733	0.711	1.782	1.297	0.240	0.372	0.388
	Image 4	1.844	1.252	2.085	1.201	0.918	2.280	0.797	0.715	1.805	1.337	0.233	0.374	0.393
	Mean	2.132	1.288	1.796	1.451	0.985	1.901	0.757	0.796	1.790	1.376	0.240	0.381	0.380
	σ	0.165	0.149	0.136	0.186	0.131	0.158	0.018	0.101	0.029	0.116	0.006	0.010	0.012
	σ (%)	7.7	11.6	7.6	12.8	13.3	8.3	2.3	12.7	1.6	8.4	2.6	2.7	3.1
M-17 wt%	Image 1	2.424	1.108	2.480	1.525	0.982	2.825	0.769	0.598	1.847	1.174	0.205	0.382	0.413
	Image 2	2.135	1.140	1.966	1.630	1.062	2.268	0.891	0.780	1.918	1.434	0.191	0.287	0.304
	Image 3	2.266	1.254	1.668	1.671	1.025	1.977	0.730	0.898	1.875	1.578	0.198	0.317	0.320
	Image 4	2.052	1.327	1.591	1.310	1.016	2.100	0.839	0.801	1.908	1.513	0.190	0.278	0.287
	Mean	2.219	1.207	1.926	1.534	1.021	2.292	0.807	0.769	1.887	1.425	0.196	0.316	0.331
	σ	0.145	0.077	0.411	0.075	0.040	0.431	0.084	0.151	0.036	0.205	0.007	0.049	0.059
	σ (%)	6.5	6.4	21.3	4.9	3.9	18.8	10.4	19.6	1.9	14.4	3.6	15.4	17.8

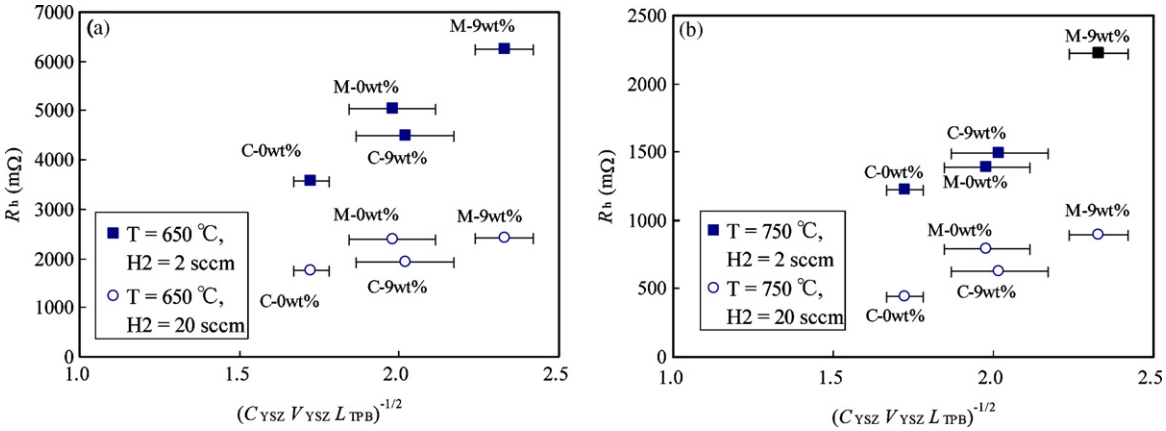

Fig. 15. R_h plotted against R.H.S. of Eq. (12). (a) 650 °C and (b) 750 °C.

where i_0 is the lineal exchange current density per unit TPB length, a is the electrode thickness, σ_{io}^{eff} and σ_{el}^{eff} are the effective ionic and electronic conductivities, respectively. Thiele modulus represents the ratio between the characteristic reactive length and the actual thickness of the electrode [26]. When anode thickness is large ($\Gamma > 3$), effective region of the electrode becomes thin and will be restricted to the vicinity of electrode/electrolyte interface. Then, the effective electrode conductance becomes inversely proportional to Γ [25]. In that case, anode conductance can be expressed using the linearized Butler–Volmer equation as:

$$\frac{1}{R} \approx i_0 L_{TPB} \frac{F}{R_0 T} a \times \frac{1}{\Gamma} = \sqrt{\frac{i_0 F L_{TPB}}{(1/\sigma_{io}^{eff} + 1/\sigma_{el}^{eff}) R_0 T}}. \quad (9)$$

From the concept of contiguity (c-c) theory [17–19], the effective conductivity of a multi-phase material (σ^{eff}) can be expressed as follows:

$$\sigma^{eff} = \sum \sigma_i C_i V_i, \quad (10)$$

where σ_i, C_i and V_i are conductivity, contiguity and volume fraction of phase i, respectively. Since ionic conductivity of Ni can be neglected, effective ionic conductivity of the Ni-YSZ cermet can be expressed as:

$$\sigma_{io}^{eff} = \sigma_{YSZ} C_{YSZ} V_{YSZ}. \quad (11)$$

Substituting Eq. (11) in Eq. (9) and neglecting electronic resistivity, the anode resistance can be related to the microstructural parameters as [27]:

$$R \approx \sqrt{\frac{(1/\sigma_{io}^{eff}) R_0 T}{i_0 F L_{TPB}}} \propto \frac{1}{\sqrt{\sigma_{io}^{eff} L_{TPB}}} \propto \frac{1}{\sqrt{C_{YSZ} V_{YSZ} L_{TPB}}}. \quad (12)$$

Fig. 15 shows the high frequency resistance R_h plotted against the R.H.S. of Eq. (12). The bars indicate the standard deviations of the four sub-regional data. For each temperature and hydrogen flow rate condition, R_h is correlated fairly well by Eq. (12). The variation of R_h with temperature and hydrogen flow rate can be attributed to the dependence of exchange current density i_0 on temperature and partial pressures of H_2 and H_2O. It is reported from the Ni pattern anode experiments that the polarization resistance is sensitive to the partial pressure of steam, P_{H_2O} [28,29]. Since local P_{H_2O} adjacent to the reactive three-phase boundary should be different for the cells with different tortuosity, exchange current density i_0 of the cells must be different even for the same temperature and bulk H_2 flow rate. Thus, quantitative discussion for the proportionality coefficient of Eq. (12) is not discussed here. However, fairly good correlation of R_h with c-c theory shown in Fig. 15 implies that the differences of anode resistances between the cells can be attributed mainly to the difference of the microstructural parameters such as contiguity, volume fraction and TPB length. Thus, it is expected that stereology and c-c theory is effective for evaluating the quantitative differences of microstructures and discussing the relationship between microstructural parameters and polarization characteristics of anode supported SOFCs.

5. Conclusions

In the present study, tubular anode supported cells with Ni-YSZ anode, YSZ electrolyte, LSM-YSZ composite cathode, and LSM cathode current collector layers were fabricated. Amount of acrylic poreformer and starting NiO-YSZ powders were varied to obtain different anode microstructures. Anode cross-section was polished by Ar-ion beam cross-section polisher and successfully imaged by low voltage SEM-EDX. Clear images of low voltage SEM-EDX made it possible to distinguish the three phases. The microstructural parameters such as TPB length, contiguity, etc. are quantified using the stereological analysis. Co-precipitated cells have good connections of Ni-YSZ and YSZ-YSZ phases, which lead to long TPB length with high porosity. On the other hand, Ni is relatively isolated and agglomerated within the pores and TPB length and porosity are small in the mechanically mixed cells. Impedance spectroscopy was performed at 650 and 750 °C with hydrogen/nitrogen mixed gas as a fuel. High frequency resistance scaled well with contiguity, volume fraction of YSZ and TPB length, i.e. $1/\sqrt{C_{YSZ} V_{YSZ} L_{TPB}}$. It is expected that stereology and c-c theory are effective for evaluating the microstructures and their polarization resistances of SOFC anodes.

Acknowledgements

This research was supported through the 21st Century COE Program, "Mechanical System Innovation," by the Ministry of Education, Culture, Sports, Science and Technology of Japan (MEXT). We would like to thank AGC Seimi Chemical Co., Ltd. and Kankyo Ceramics Research Co., Ltd. for supplying original powders and extruded tubes and for the beneficial discussions.

References

[1] S.C. Singhal, K. Kendall, High Temperature Solid Oxide Fuel Cells, Elsevier, 2002.
[2] J.-H. Kim, R.-H. Kim, K.-S. Song, S.-H. Hyun, D.-R. Shin, H. Yokokawa, J. Power Sources 122 (2003) 138–143.
[3] T. Suzuki, T. Yamaguchi, Y. Fujishiro, M. Awano, J. Electrochem. Soc. 153 (3) (2006) A925–A928.
[4] J. Pusz, A. Mohammadi, N.M. Singhal, ASME J. Fuel Cell Sci. Technol. 3 (2006) 482–486.

[5] M. Mogensen, S. Skaarup, Solid State Ionics 86–88 (1996) 1151–1160.
[6] H. Koide, Y. Someya, T. Yoshida, T. Maruyama, Solid State Ionics 132 (2000) 253–260.
[7] A. Atkinson, S. Barnett, R.J. Gorte, J.T.S. Irvine, A.J. Mcevoy, M. Mogensen, S.C. Singhal, J. Hohs, Nat. Mater. 3 (2004) 17–27.
[8] H. Abe, K. Murata, T. Fukui, W.-J. Moon, K. Kaneko, M. Naito, Thin Solid Films 496 (2006) 49–52.
[9] T. Fukui, K. Murata, S. Ohara, H. Abe, M. Naito, K. Nogi, J. Power Sources 125 (2004) 17–21.
[10] H. Itoh, T. Yamamoto, M. Mori, T. Horita, N. Sakai, H. Yokokawa, M. Dokiya, J. Electrochem. Soc. 144 (2) (1997) 641–646.
[11] Y.-J. Leng, S.-H. Chan, K.-A. Khor, S.-P. Jiang, P. Cheang, J. Power Sources 117 (2003) 26–34.
[12] S.-D. Kim, H. Moon, S.-H. Hyun, J. Moon, J. Kim, H.-W. Lee, Solid State Ionics 177 (2006) 931–938.
[13] J.-H. Yu, G.-W. Park, S. Lee, S.-K. Woo, J. Power Sources 163 (2007) 926–932.
[14] J.R. Wilson, W. Kobsiriphat, R. Mendoza, H.-Y. Chen, J.M. Hiller, D.J. Miller, K. Thornton, P.W. Voorhees, S.B. Adler, S. Barnett, Nat. Mater. 5 (2006) 541.
[15] J.R. Izzo Jr., A.S. Joshi, K.N. Grew, W.K.S. Chiu, A. Tkachuk, S.H. Wang, W. Yun, J. Electrochem. Soc. 155 (5) (2008) B504–B508.
[16] R.T. DeHoff, F.N. Rhines, Quantitative Microscopy, McGraw-Hill, 1968.
[17] J. Gurland, Trans. Metall. Soc. AIME 236 (1966) 642–646.
[18] Z. Fan, A.P. Miodownik, P. Tsakiropoulos, Mater. Sci. Technol. 9 (1993) 1094–1100.
[19] D. Simwonis, F. Tiez, D. Stöver, Solid State Ionics 132 (2000) 241–251.
[20] J.-H. Lee, H. Moon, H.-W. Lee, J. Kim, J.-D. Kim, K.-H. Yoon, Solid State Ionics 148 (2002) 15–26.
[21] D.-S. Lee, J.-H. Lee, J. Kim, H.-W. Lee, H.S. Song, Solid State Ionics 166 (2004) 13–17.
[22] K.-R. Lee, S.-H. Choi, H.-W. Lee, J.-H. Lee, J. Power Sources 140 (2005) 226–234.
[23] K.-R. Lee, Y.S. Pyo, B.S. So, S.M. Kim, B.K. Lee, J.H. Hwang, J. Kim, J.-H. Lee, H.-W. Lee, J. Power Sources 158 (2006) 45–51.
[24] R. Barfod, M. Mogensen, T. Klemenso, A. Hagen, Y.-L. liu, P.V. Hendriksen, J. Electrochem. Soc. 154 (4) (2007) B371–B378.
[25] P. Costamagna, P. Costa, V. Antonucci, Electrochim. Acta 43 (3–4) (1998) 375–394.
[26] P. Costamagna, P. Costa, E. Arato, Electrochim. Acta 43 (8) (1998) 967–972.
[27] Y. Suzue, N. Shikazono, N. Kasagi, J. Power Sources 184 (2008) 52–59.
[28] J. Mizusaki, H. Tagawa, T. Saito, T. Yamamura, K. Kamitani, K. Hirano, S. Ehara, T. Takagi, T. Hikita, M. Ippommatsu, S. Nakagawa, K. Hashimoto, Solid State Ionics 70/71 (1994) 52–58.
[29] A. Bieberle, L.P. Meier, L.J. Gauckler, J. Electrochem. Soc. 148 (6) (2001) A646–A656.